Detrended fluctuation analysis in x-ray photon correlation spectroscopy for determining coarsening dynamics in alloys

Lorenz-M. Stadler,[1,*] Bogdan Sepiol,[1] Bastian Pfau,[1] Jan W. Kantelhardt,[2] Richard Weinkamer,[3] and Gero Vogl[1]
[1]*Fakultät für Physik, Institut für Materialphysik, Universität Wien, Strudlhofgasse 4, A-1090 Wien, Austria*
[2]*Fachbereich Physik und Zentrum für Computational Nanoscience, Martin-Luther-Universität Halle-Wittenberg, D-06099 Halle, Germany*
[3]*Max Planck Institute of Colloids and Interfaces, Research Campus Golm, D-14424 Potsdam, Germany*
(Received 29 March 2006; revised manuscript received 14 July 2006; published 6 October 2006)

We study the *dynamics* of precipitate coarsening in phase-separating alloys at late stages of phase separation by x-ray photon correlation spectroscopy (XPCS). For analyzing time series of fluctuating speckle intensities from small-angle scattering of coherent x rays, the method of detrended fluctuation analysis (DFA), which is ideal for determining power-law correlations, is applied. We discuss the application of DFA with respect to XPCS data by means of simulated time series. In particular, the effects of different signal-to-noise ratios are examined. Results from measurements of the two model systems Al-6 at. % Ag at 140 °C and Al-9 at. % Zn at 0 °C are presented. Since the DFA effectively removes adulterating trends in the data, quantitative agreement with Monte Carlo simulations is obtained. It is verified that two different coarsening mechanisms are predominant in the two systems—coarsening either by diffusion of single atoms or by movement of whole precipitates.

DOI: 10.1103/PhysRevE.74.041107 PACS number(s): 05.40.−a, 61.10.Eq, 81.05.Bx

I. INTRODUCTION

Late stages of phase separation in alloys are characterized by coarsening of precipitates in order to reduce excess interfacial energy. The usual textbook explanation of how the precipitate coarsening proceeds is the classical Lifshitz-Slyozov-Wagner (LSW) mechanism [1,2], where atoms evaporate from smaller precipitates, diffuse through the matrix, and condense on larger precipitates. The diffusion process, however, is strongly dependent on the exact interplay between vacancies and the different atom species [3]. Detailed Monte Carlo studies [4,5] showed that if vacancies are preferably located in the matrix, the diffusion of single atoms is fostered and the LSW mechanism dominates the coarsening dynamics. If, on the other hand, vacancies are preferentially found in the precipitates or on their surfaces, the precipitates can move as a whole and eventually coalesce. Thus, precipitate coagulation may also be a predominant coarsening mechanism in solids, as was suggested earlier [6].

To experimentally distinguish between the different coarsening mechanisms is difficult. One common approach is to attribute the coarsening mechanism to the observed growth law. One major result of the LSW theory is that asymptotically ($t \to \infty$) the growth of the mean precipitate radius $\langle R(t) \rangle$ is described by a power law $\propto t^{\Lambda}$ with $\Lambda = 1/3$. Thereby, a highly diluted system with an infinitely small precipitate volume is assumed. Basically, theories that take into account a finite precipitate volume reproduce $\Lambda = 1/3$ as growth exponent; compare Ref. [7], for instance. For precipitate coagulation [6,8], on the other hand, the growth exponent Λ was evaluated between $\Lambda = 1/6$ and $1/4$. From the experimental point of view, however, it does not appear feasible to decide merely on the basis of the measured time exponent whether a coagulation mechanism influences the coarsening *kinetics* of the precipitate microstructure [9]. Also, the actual structure function obtained in scattering experiments, which gives a *static* picture of the instantaneous mean precipitate arrangement, does not allow for discriminating between different coarsening mechanisms [5].

An alternative and promising approach is to study *in situ* the coarsening *dynamics* with the emerging method of x-ray photon correlation spectroscopy (XPCS), which has become feasible with the advent of third-generation synchrotron sources. In contrast to electron microscopy investigations, information about processes in a large sample volume is gained. XPCS relies on the fact that scattering of coherent radiation from a disordered sample produces a highly modulated diffraction pattern, commonly referred to as speckle pattern [10]. This interference pattern is in direct relation to the positions of all scattering centers in the coherently illuminated material. If their positions change, the corresponding speckle pattern will also be modified, and the intensity of the speckles will fluctuate in time. Measuring this intensity for a certain scattering vector $\boldsymbol{Q}$ involves a time average $\langle I(\boldsymbol{Q},t) \rangle_T$ taken over the acquisition time T, but does not include an ensemble average, as would be the case for incoherent scattering. Only if the system is ergodic, i.e., fluctuations are on a time scale much shorter than the counting time and the measured time average is equivalent to an ensemble average, can $\langle I(\boldsymbol{Q},t) \rangle_T$ be replaced by the usual ensemble average, denoted by $\langle I(\boldsymbol{Q},t) \rangle$. In the latter case, the observed scattering is featureless apart from time-averaged correlations in the sample, similar to every scattering experiment with incoherent radiation. If, however, the dynamics is slower than the acquisition time T, the measurement of the intensity fluctuations of speckles can reveal the dynamics of the system. This is done by analyzing the temporal correlations contained in the measured signal. By using coherent x rays, atomic resolution can almost be achieved [11].

*Electronic address: Lorenz-Mathias.Stadler@univie.ac.at

In the aforementioned Monte Carlo study by Weinkamer and Fratzl [5], time-dependent speckle intensities, corresponding to an XPCS experiment in small-angle x-ray scattering (SAXS) geometry, were simulated for coarsening via the classical LSW mechanism as well as for predominating precipitate coagulation. The fluctuating speckle intensities were analyzed by fluctuation analysis (FA) and turned out to be power law correlated. The detected correlation behavior was dependent on the scattering vector—in a characteristic way for each coarsening mechanism. In a recent XPCS experiment, Al-6 at. % Ag at 140 °C and Al-9 at. % Zn at 0 °C were measured and the data were analyzed by means of FA and compared to the simulation results [5], which were published as a Rapid Communication [12]. A qualitative agreement was found between the data for Al-6 at. % Ag at 140 °C and the LSW mechanism. For Al-9 at. % Zn at 0 °C, the results indicated coagulation of whole precipitates as the dominant coarsening mechanism.

In this paper, we extend the analysis of our data to *detrended* fluctuation analysis (DFA) for both the simulation and the experimental results in order to better quantify the obtained temporal power-law correlations. Using DFA instead of FA enables us to remove trends that adulterate the correlation behavior from our data, and quantitative agreement between simulation and the experiment is found.

The paper is organized as follows. In Sec. II, we introduce FA and DFA, respectively, as the method of choice for analyzing power-law correlations. We further discuss FA and in particular DFA for analyzing XPCS data. In Sec. III, experimental details are given. Results and discussion are found in Sec. IV.

II. ANALYZING CORRELATIONS IN XPCS TIME SERIES

The common way to analyze data of an (X)PCS experiment is to calculate a correlation function of the temporal fluctuating intensity measured at a certain scattering vector $\boldsymbol{Q}$. In the case of equilibrium systems, the dynamics depends only on relative times (time lags) t and the computation of the normalized intensity-autocorrelation function $g^{(2)}(t)$ is sufficient. If one measures the speckle intensity at N discrete time steps k, $g^{(2)}(t)$ is calculated as

$$g^{(2)}(t) = \frac{\frac{1}{N-t}\sum_{k=1}^{N-t} \Delta I_k \Delta I_{k+t}}{\langle I \rangle^2}, \tag{1}$$

with discrete time lags $t=0,\ldots,N-1$, I_k the intensity in the kth time bin, and intensity fluctuations ΔI_k. The latter are given by

$$\Delta I_k = I_k - \langle I \rangle, \quad \text{where } \langle I \rangle = \frac{1}{N}\sum_{k=1}^{N} I_k. \tag{2}$$

Note that in the case of nonequilibrium systems, the dynamics depends on the absolute time. Thus, it is not sufficient to consider relative time intervals by calculating the autocorrelation function of the signal. Instead, a two-time correlation function is typically used. In recent papers, that approach was chosen for studying phase-ordering [13,14] and phase-separating systems [15], respectively.

The autocorrelation-function technique is particularly suited for revealing short-term correlations like an exponential decay of $g^{(2)}(t)$. Typically, the latter occurs for Brownian motion in colloidal suspensions [16–18], i.e., in dependence on the scattering vector, $g^{(2)}(t) \propto \exp(-t/\tau_c)$ is found and correlation times τ_c are gained.

The situation, however, changes if long-term power-law correlations have to be resolved, implying

$$g^{(2)}(t) \propto t^{-\gamma} \quad \text{with } 0 < \gamma < 1. \tag{3}$$

In particular, on longer time scales $g^{(2)}(t)$ becomes statistically unreliable. Furthermore, it shows artifacts in the presence of trends, caused, for example, by an unstable overall intensity during the measurement time. In general, a "trend" is a *systematic* change of the mean of a time series. In data with a trend, the autocorrelation function is no longer defined, actually. More generally speaking, a time series becomes nonstationary if the mean or the variance or other important statistical properties like autocorrelations change with time. Nonstationarities are often caused by extrinsic processes.

The problem of statistical accuracy can be avoided by using fluctuation analysis (FA). Furthermore, FA can easily be extended to detrended fluctuation analysis (DFA), which makes it possible to circumvent the problem of trends. Both FA and DFA are techniques that were originally introduced for the determination of long-range correlations in the sequence of base pairs in the DNA [19,20] and were further successfully applied to, e.g., the analysis of climate records [21], heartbeat time series during sleep [22], and economical time series [23].

In calculating the (D)FA, we consider the integrated time series or "profile"

$$Y(j) = \sum_{k=1}^{j} \Delta I_k. \tag{4}$$

In the case of FA, the so-called fluctuation function $F(t)$ is given by

$$F(t) = \sqrt{\langle [Y(j+t) - Y(j)]^2 \rangle}, \tag{5}$$

where the angle brackets represent an average over all pairs with the same time lag t. In the case of DFA, the profile, Eq. (4), is divided into nonoverlapping segments of size t, where t will be the scaling variable, i.e., the aim is to measure the fluctuations on the time scale t while simultaneously eliminating trends ("detrending" of the data). For DFA of order n (DFAn), in each segment $Y(j+1)$ to $Y(j+t)$ [or equivalently $Y(j+i)$ with $i=1,\ldots,t$], the best fit of a polynomial $p_j(i)$ of order n is determined. In this way, trends of order n in the profile and of order $n-1$ in the raw data, respectively, are removed [24]. In practice, it is mostly sufficient to use DFA3, and higher orders need not be calculated [25]. In the following, we thus concentrate on third-order detrended fluctuation analysis when discussing the evaluation of our XPCS data.

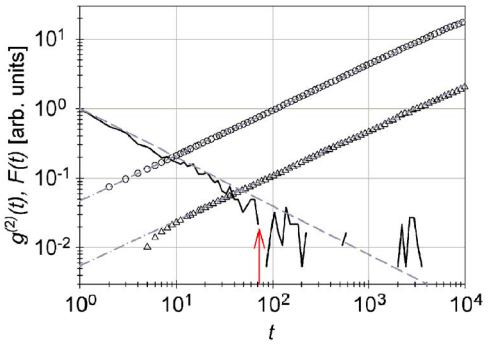

FIG. 1. (Color online) Analysis of simulated power law-correlated data (γ=0.7) with the classical autocorrelation function $g^{(2)}(t)$ (solid black line) and the fluctuation function $F(t)$ calculated with FA (open circles) and DFA3 (open triangles), respectively. Double-logarithmic plot. Curves are shifted along the y axis for clarity. The red arrow marks the point where the autocorrelation function becomes negative for the first time. The scaling behavior on longer time scales is completely inaccessible in that approach. The dashed gray line indicates γ=0.7. A reasonable fit is hardly possible. (D)FA, on the other hand, yields the correct scaling behavior over many orders of magnitude. The dash-dotted gray lines indicate α=0.65, compare Eq. (7), which can be perfectly fitted.

In the next step, the variance of the profile $Y(j+i)$ from the polynomial $p_j(i)$ is calculated,

$$F_j^2(t) = \frac{1}{t}\sum_{i=1}^{t} [Y(j+i) - p_j(i)]^2. \tag{6}$$

$F_j^2(t)$ is averaged over all segments and finally the square root is taken to get $F(t)$.

To gain information about the correlations in the intensity fluctuations, the scaling behavior of the fluctuation function has to be analyzed. $F(t)$ is fitted by a power law $F(t) \propto t^{\alpha}$, with α the so-called fluctuation exponent, which is a measure for the degree of correlation or persistence in the system. Thereby, "persistence" denotes the tendency of a random variable to keep its actual value. In analogy to random-walk theory, $\alpha = 1/2$ is found for uncorrelated data and $\alpha > 1/2$ for data containing long-term correlations [24,25]. The fluctuation exponent α is related to the correlation exponent γ, compare Eq. (3), by

$$\alpha = 1 - \gamma/2. \tag{7}$$

Before coming to a more detailed interpretation of $F(t)$, it is instructive to have a look at an example that illustrates the application of (D)FA to power-law correlated data in comparison with the autocorrelation function approach. For that purpose, a series of long-range correlated random numbers with a correlation exponent γ=0.7 was generated with a Fourier filtering method. A brief description of that method together with an advanced algorithm for generating long-range correlations for large systems can be found in Ref. [26]. Figure 1 shows the autocorrelation function of those data as well as fluctuation functions obtained from FA and DFA3 evaluations in a double-logarithmic plot.

Clearly, the autocorrelation function fails to characterize the correlation behavior on longer time scales. The correct scaling behavior (γ=0.7) is indicated only on relatively short time scales, see the dashed gray line for comparison, but even there a reasonable fit is not a trivial task. The fluctuation functions, on the other hand, yield the correct long-term correlations with slopes in the double-logarithmic plot of α =0.65 (indicated by the dash-dotted gray lines) over many orders of magnitude, even at late times. Only the first few points of the DFA3 curve do not lie on the corresponding straight in the double-logarithmic plot, which is an artifact caused by the construction of the DFA-fluctuation functions [24]. Fitting the correct fluctuation exponent α is thus easily possible.

The interpretation of the resulting fluctuation function can be understood in analogy to the random walk of a particle in one dimension in space. If ΔI_k in Eq. (4) denoted the (uncorrelated) *step* of the particle at time step k, the profile $Y(j)$ would correspond to the position of the random walker after j time steps. Furthermore, Eq. (5) would describe its root-mean-square displacement after t steps. According to Einstein, the root-mean-square displacement $\sqrt{\langle x^2 \rangle}$ of a random walker grows with the square root of time,

$$\sqrt{\langle x^2 \rangle} = \sqrt{2D_0 t}, \tag{8}$$

with D_0 the diffusion coefficient. Hence, if there are no correlations present in the XPCS data, we expect

$$F(t) \propto t^{\alpha} \quad \text{with } \alpha = 1/2. \tag{9}$$

If, on the other hand, the diffusion became anomalous, i.e., if the random walk were accelerated on all time scales ("superdiffusion"), the movement of the random walker would become long-term correlated and its root-mean-square displacement would grow faster than with the square root of time, yielding $\alpha > 0.5$. Hence, if there are (long-term) correlations in our XPCS data, we expect

$$F(t) \propto t^{\alpha} \quad \text{with } \alpha > 1/2. \tag{10}$$

Note that by construction the maximum α value detectable with FA is $\alpha_{\max}=1$, whereas DFAn can resolve $\alpha_{\max} = 1+n$ [24]. This is of importance when the correlation behavior becomes nonstationary. In an XPCS experiment, $\alpha > 1$ can be caused by a strong persistence in the investigated system, which gives rise to quite monotonic increase or decrease of the measured intensity over longer time segments. In addition, trends in the data can lead to spurious results with $\alpha > 1$. Successively applying DFA of higher order removes these trends, i.e., only the real scaling behavior remains.

An example for $\alpha > 1$ that can be simulated easily is random-walk dynamics, where $\alpha = 3/2$ is obtained [25]: If the ΔI_k in Eq. (4) were already given by a random walk, i.e., if they corresponded to the *position* of a diffusing particle, the mean of ΔI_k itself would increase as $\langle \Delta I_k \rangle \propto k^{1/2}$. In this case, the calculation of the profile in Eq. (4) involves an additional summation over time (or integration if considered as a continuous process). This integration increases the scaling exponent α by 1, leading to

$$F(t) \propto t^{\alpha} \quad \text{with } \alpha = 3/2. \tag{11}$$

Concerning the interpretation of fluctuation functions calculated from XPCS data, there are three other issues of which one must be aware. First, although intensities are measured, it is phase information that is retrieved, because the phasing of the scattered photons determines the detected intensity fluctuations. In principle, any phase information is modulo 2π. Due to the dynamics in the sample, the phase of the scattered photons changes temporally. Hence, e.g., for random-walk dynamics, we can expect $\alpha=3/2$ in principle and $\alpha=1$ for the restricted FA fluctuation functions, respectively. However, after an additional phase difference of 2π between interfering scattered waves is exceeded, the situation becomes indistinguishable from the initial state. Thus, if the dynamics is sufficiently fast, $\alpha>1/2$ will not be observed on very large time scales. Second, when detecting single photons, the measurement is accompanied by shot noise. The question is how this statistical noise affects the fluctuation functions. And third, in the experiment the signal-to-noise ratio is further deteriorated by the limited coherence of real x-ray beams.

In the following, we use simulated data for a random walk of phases to illuminate the above points. The variable x_k denotes the position of a *single* random walker in one dimension at time step k and is recursively defined by $x_k=x_{k-1}+r_k$, with $x_0=0$ and uncorrelated random numbers (steps) r_k (continuous distribution $-0.1<r_k<0.1$). The corresponding instantaneous scattering intensity in an XPCS experiment with perfect coherence conditions will be $I_{\max}^{\mathrm{coh}} \sin^2 x_k$, with $I_{\max}^{\mathrm{coh}}$ the maximum coherent intensity. However, since single photons are registered in the experiment instead of continuous intensities, the measurement result is affected by shot noise. In order to account for the shot noise at each time step, $I_{\max}^{\mathrm{coh}} \sin^2 x_k$ is not considered, but rather a random number from a (discrete) Poisson distribution with mean $\xi = I_{\max}^{\mathrm{coh}} \sin^2 x_k$. The random variable representing the number of photon counts at time step k is thus

$$I_k = [I_{\max}^{\mathrm{coh}} \sin^2 x_k]_{\mathrm{PD}}, \tag{12}$$

with $[\xi]_{\mathrm{PD}}$ denoting a random number from a Poisson distribution with mean ξ. Note that in reality not only are the detected numbers of scattered photons Poisson-distributed, but also the intensity of the incoming x-ray beam obeys Poisson statistics, since the generation of x rays in a synchrotron is a random process. Furthermore, the intensity distribution for scattering of perfectly coherent photons at a disordered material obeys negative exponential statistics [27]. For the sake of clarity and simplicity, these additional distributions are omitted here. In modeling data for tests of the DFA analysis, there is no need to simulate the exact distribution of the data. We only need to simulate a realistic correlation behavior, because DFA results are rather independent of the exact distribution of the intensities as long as their moments do not diverge.

Figure 2 shows resulting DFA3 fluctuation functions for time series generated according to Eq. (12) with different maximum coherent intensities that range from $I_{\max}^{\mathrm{coh}}=10^{-2}$ (♦) to $I_{\max}^{\mathrm{coh}}=10^{4}$ (●). Due to the Poisson statistics,

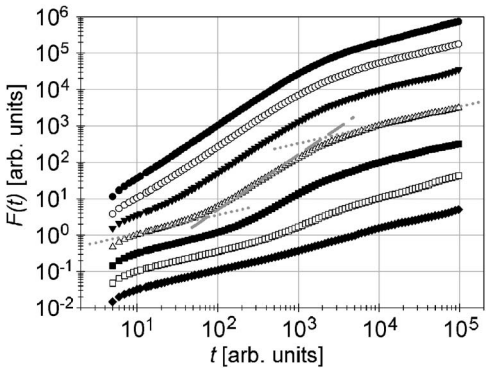

FIG. 2. Illustration of the effect of Poisson noise on DFA3 curves by means of simulated random walks of phases according to Eq. (12). $I_{\max}^{\mathrm{coh}}=10^4$ (●), 10^3 (○), 10^2 (▼), 10^1 (△), 10^0 (■), 10^{-1} (□), and 10^{-2} (♦). Perfect coherence conditions are assumed, i.e., no incoherent background is present. Double-logarithmic plot. Curves are shifted along the y axis for clarity. Dotted gray lines indicate slope 1/2 and the dashed gray line corresponds to $\alpha=3/2$.

the curves correspond to cases with different signal-to-noise ratios. Each curve represents an average over 10 runs with 10^5 time steps each.

For high intensities [$I_{\max}^{\mathrm{coh}}=10^4$ (●) and $I_{\max}^{\mathrm{coh}}=10^3$ (○)] with a relatively low Poisson noise, the fluctuation functions exhibit $\alpha=3/2$ followed by a crossover to $\alpha=1/2$ at $t \approx 3000$. This crossover is solely determined by how fast the random walk of phases advances. The crossover time $\tau \approx 3000$ corresponds to the time needed for the random walk to increase or decrease by π, because π is the period for the intensity. This implies a root-mean-square displacement of $\sqrt{\langle x^2(\tau)\rangle}=\pi$. Since the mean-square step width of the random walk is $2D_0=\langle r^2\rangle$ and

$$\langle r^2\rangle = \frac{1}{0.2}\int_{-0.1}^{0.1} r^2\, dr = \frac{1}{300}, \tag{13}$$

we obtain $\tau=\langle x^2(\tau)\rangle/(2D_0)=300\pi^2\approx 3000$.

For lower intensities with increasing Poisson noise, $\alpha=1/2$ is also found on short time scales, followed by a crossover to $\alpha=3/2$, and finally by the crossover back to $\alpha=1/2$ at $t\approx\tau$. The first crossover (from $\alpha=1/2$ to 3/2) is similar to the crossover observed in long-term correlated data with additional large uncorrelated spikes [28], although it is caused here by additional random fluctuations due to the stationary, i.e., continuously present, shot noise. The crossover is shifted to longer time scales with increasing shot noise (decreasing intensity). While there is no problem for intermediate and moderate intensities, the shift of the first crossover makes the detection of the correct scaling behavior quite difficult for low intensities [$I_{\max}^{\mathrm{coh}}=10^{-1}$ (□)] and even impossible for very low intensities [$I_{\max}^{\mathrm{coh}}=10^{-2}$ (♦)].

In real experiments, the signal-to-noise ratio is further limited by nonperfect coherence properties of the used x-ray beam, causing a limited speckle contrast (or "visibility"). The question arises whether DFA fluctuation functions from such data can be reasonably evaluated. In order to answer

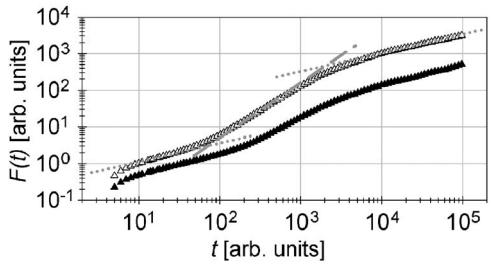

FIG. 3. Illustration of the effect of Poisson noise plus an additional incoherent background, $I_{\mathrm{av}}^{\mathrm{inc}}$, on DFA3 curves by means of simulated random walks of phases according to Eq. (14). (△): $I_{\mathrm{max}}^{\mathrm{coh}}=10$, $I_{\mathrm{av}}^{\mathrm{inc}}=0$. (▲): $I_{\mathrm{max}}^{\mathrm{coh}}=10$, $I_{\mathrm{av}}^{\mathrm{inc}}=45$. Double-logarithmic plot. Curves are shifted along the y axis for clarity. Dotted gray lines indicate slope 1/2 and the dashed gray line corresponds to $\alpha=3/2$.

this question, we extend our example of a random walk of phases by introducing a mean "incoherent" background $I_{\mathrm{av}}^{\mathrm{inc}}$. The simulated count number at time step k then reads

$$I_k = [I_{\mathrm{max}}^{\mathrm{coh}} \sin^2 x_k + I_{\mathrm{av}}^{\mathrm{inc}}]_{\mathrm{PD}}, \tag{14}$$

with $I_{\mathrm{av}}^{\mathrm{inc}}$ the mean incoherent background. Again, in the modeling of the intensity correlation behavior for our DFA study, the exact intensity statistics for scattering of partially coherent photons, which can be described by a gamma distribution [27], is not taken into account for the sake of clarity and simplicity. For a detailed discussion of how partial coherence affects measured x-ray speckle patterns, see, e.g., Refs. [29–31].

If we chose $I_{\mathrm{max}}^{\mathrm{coh}}=10$ and $I_{\mathrm{av}}^{\mathrm{inc}}=45$, we have a mean coherent intensity of

$$I_{\mathrm{av}}^{\mathrm{coh}} = \frac{1}{2\pi}\int_0^{2\pi} I_{\mathrm{max}}^{\mathrm{coh}} \sin^2 x \, dx = 5 \tag{15}$$

and thus a coherent fraction of 10%. In our experiment, the contrast β, i.e., the instantaneous coherence, was estimated as $\beta \approx 12\%$; see Sec. III for details. Note that the contrast depends on the actual setup and may thus vary from experiment to experiment. For example, Livet *et al.* reported $\beta \approx 25\%$ when they studied unmixing in an Al-Li alloy with XPCS [15]. The following considerations can thus be regarded as reasonable assessment.

The coherent fluctuations are estimated by the standard deviation

$$\sigma_{\mathrm{coh}} = \sqrt{\frac{1}{2\pi}\int_0^{2\pi} (I_{\mathrm{max}}^{\mathrm{coh}} \sin^2 x - I_{\mathrm{av}}^{\mathrm{coh}})^2 \, dx} = \frac{5}{\sqrt{2}}. \tag{16}$$

This means that although the coherent fraction is only 10%, the fraction of coherent fluctuations is still 50%, since we find for the relation between σ_{coh} and the overall Poisson noise σ_P

$$\frac{\sigma_{\mathrm{coh}}}{\sigma_P} = \frac{5}{\sqrt{2}\sqrt{50}} = \frac{1}{2}. \tag{17}$$

Figure 3 shows the resulting fluctuation function (▲) in comparison with the fluctuation function without an incoherent background.

As can be seen, the first crossover is further shifted to longer time scales. Although further reduced, the region with $\alpha=3/2$ is still accessible and hence DFA can be used to analyze the scaling behavior. Note that in the case of very slow dynamics, the second crossover from $\alpha=3/2$ to 1/2 would not be seen and the application of DFA would be even more reasonable.

III. EXPERIMENTAL DETAILS

The XPCS experiments were performed at the undulator beamline ID10A at the European Synchrotron Radiation Facility, Grenoble [29] in SAXS (transmission) geometry with the two phase-separating systems, Al-6 at. % Ag at 140 °C and Al-9 at. % Zn at 0 °C. Both are well-known model systems for precipitate growth [32–35], where the minority component forms precipitates. Due to small lattice misfits, spherical precipitates with the same lattice structure as the matrix are found. In the case of the Al-Zn system, size effects can cause a precipitate anisotropy [36]. However, in the experiments carried out in the frame of the study at hand, possible local anisotropies could not be detected within the measured Q range. Both systems show a self-similar evolution of the microstructure, i.e., without an absolute gauge it is not possible to determine whether the coarsening process has just started or is already in a very late stage. This implies a scaling structure function, $S(Q,t)$ [32,35]. When scaled to the Q value of the occurring peak in the small-angle scattering curve, Q_{max}, the scattering function becomes time-independent.

Evaluating the reduced temperature T/T_c, where the critical temperature for the miscibility gap, T_c, is taken from the equilibrium phase diagram, yields ≈0.55 for the Al-6 at. % Ag and ≈0.61 for the Al-9 at. % Zn measurement. This means that the measurements are both well comparable between each other and performed at reduced temperatures where no coarsening mechanism is excluded by theory [37].

To ensure that our samples were in the coarsening regime of phase separation, samples were first homogenized for 48 h at 550 °C (Al-6 at. % Ag) and for 135 min at 400 °C (Al-9 at. % Zn), respectively. Afterwards, Al-6 at. % Ag was annealed at the measurement temperature of 140 °C for 47 h, Al-9 at. % Zn at 0 °C for 82 h. In contrast to recent measurements of Livet *et al.* [15] and Malik *et al.* [38], respectively, our experiments were performed in quasiequilibrium, i.e., the sample temperature was low enough to prevent significant precipitate growth during a single measurement, which lasted a few hours. In all cases, SAXS-diffraction patterns taken before and after the XPCS measurements did not show any change, i.e., the mean precipitate size did not change measurably. For estimating the mean-precipitate radius $\langle R \rangle$, a Guinier analysis [39] was performed on the high angle side of the scattering function [40,41] ($Q > Q_{\mathrm{max}}$), yielding $\langle R \rangle \approx 8.5$ nm for Al-6 at. % Ag and $\langle R \rangle \approx 3.0$ nm for Al-9 at. % Zn.

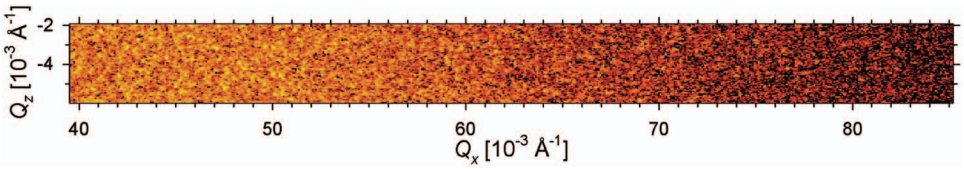

FIG. 4. (Color) Typical region of interest of the SAXS-diffraction pattern of the Al-9 at. % Zn sample at 0 °C. Logarithmic pseudocolor-intensity scale from 1 to 35 photons (dark to bright). For improving statistics, the sum of 10 frames (1 s exposure each) is shown, where a dark file was subtracted from each frame before summing. Since the coarsening dynamics was very slow, the speckle structure ("graininess") is clearly visible and not washed out.

The x-ray energy, selected by a Si(111) monochromator, was 8 keV, corresponding to a wavelength of $\lambda=1.55$ Å. An energy resolution of $\Delta E/E=1.4\times10^{-4}$ provided the temporal coherence. Since the XPCS experiments were done in SAXS geometry, the maximum path-length difference of scattered photons was well below the limit set by the longitudinal coherence length of $\xi_l\approx\lambda^2/\Delta\lambda\approx1.11$ μm. A circular pinhole aperture of diameter $d=12$ μm approximately 20 cm upstream of the sample was used to constrain the beam to a spatially coherent cross section, approximately. A guard slit in front of the sample was used to eliminate parasitic scattering from the pinhole.

For determining the contrast β, the intensity statistics of a (partially coherent) experimental speckle pattern was analyzed. The same methods as described in Refs. [29,30] were applied. First, the probability density of the speckle intensity was calculated and analyzed, assuming that the observed speckle pattern was the intensity sum of M independent speckle patterns, implying $\beta=1/M$. Second, a normalized two-point correlation function

$$C(\boldsymbol{r}_1,\boldsymbol{r}_2)=\frac{\langle I(\boldsymbol{r}_1)I(\boldsymbol{r}_2)\rangle}{\langle I(\boldsymbol{r}_1)\rangle\langle I(\boldsymbol{r}_2)\rangle} \tag{18}$$

was calculated, where $\boldsymbol{r}_{1,2}$ are points in the detector image plane and the angle brackets indicate a spatial average over the region of interest. In the limit of zero pixel separation, this correlation function is $1+\beta$. Both methods yielded the same result $\beta\approx12\%$ within the error bars.

For optimizing the SAXS signal, sample thicknesses were 46 μm for Al-6 at. % Ag and 70 μm for Al-9 at. % Zn, respectively, corresponding to an intensity transmission of $1/e$ each. The Al-6 at. % Ag sample was measured in an evacuated transmission furnace with kapton windows, whereas the Al-9 at. % Zn sample was mounted on a cooling tip that was kept at ice-water temperature.

Time series of up to $N=8192$ speckle patterns ("frames") were taken with a direct-illumination CCD camera (Princeton Instruments, 1242×1152 pixels, pixel size 22.5×22.5 μm^2) mounted on a table at a distance of $L=2.3$ m from the sample. Since the estimated speckle size was $\approx L\lambda/d=29.7$ μm, the spatial resolution of the detector was high enough to resolve the speckle structures. As shown in Ref. [12], ring-like SAXS patterns were obtained, caused by isotropic shape and arrangement of the precipitates. When measuring near the SAXS maximum, which defined $Q_{\max}$, the exposure time was typically 1 s. To save readout time and to cover the largest possible range of the scattering vector Q, rectangular regions of interest with $\Delta Q_x\gg\Delta Q_z$ were chosen, thus allowing for a total repetition rate of one frame per 1.65 s, typically. Due to the isotropy of the SAXS signal, no loss of information occurred. Since the whole CCD detector covered a maximum Q range of 0.049 Å^{-1}, up to three consecutive measurements with different, slightly overlapping positions of the CCD camera were performed. The maximum Q range accessible was limited to about 0.18 Å^{-1}, due to insufficient scattering intensity for larger Q.

For comparison with the experiments, we have performed Monte Carlo simulations on an fcc lattice, where the 128^3 sites were occupied by two species of atoms and a vacancy [5]. Considering a pairwise interaction between the atoms, the Hamiltonian can be written as an extended Ising model with two parameters. The ordering energy J defines the interaction between the atoms and was chosen to induce phase separation. Important for this work is the asymmetry parameter U, which characterizes the interaction between the vacancy and the atoms and thus determines the preferred location of the vacancy. It was shown [5] that the choice $U=+J$ results in a preferred location of the vacancy inside the precipitates, leading to coarsening via precipitate coagulation. With the second investigated choice $U=-J$, the vacancy prefers the matrix and coarsening proceeds via the LSW mechanism. Changes in the configuration were performed by exchanges of the vacancy with neighboring atoms (vacancy dynamics) using a standard METROPOLIS algorithm. Further details of the simulation procedure can be found in Ref. [5]. For the XPCS computer experiment, the scattering intensity was determined at 100 equidistant time steps, where the low number of time steps guarantees quasiequilibrium conditions also in the simulation. The interval between two time steps was chosen to allow for a close comparison with the XPCS measurements.

IV. RESULTS AND DISCUSSION

Figure 4 shows a speckled SAXS pattern of the Al-9 at. % Zn sample, where the maximum of the scattering function is visible at the left side of the frame.

For improving statistics, 10 frames (1 s exposure each) were summed, and since the coarsening dynamics was very slow, the speckle structure is clearly visible and not washed out. Before summing, a dark file was subtracted from each frame in order to get rid of the dark current of the CCD. As a dark file, the average of 30 dark pictures, i.e., frames taken with x rays off, was used.

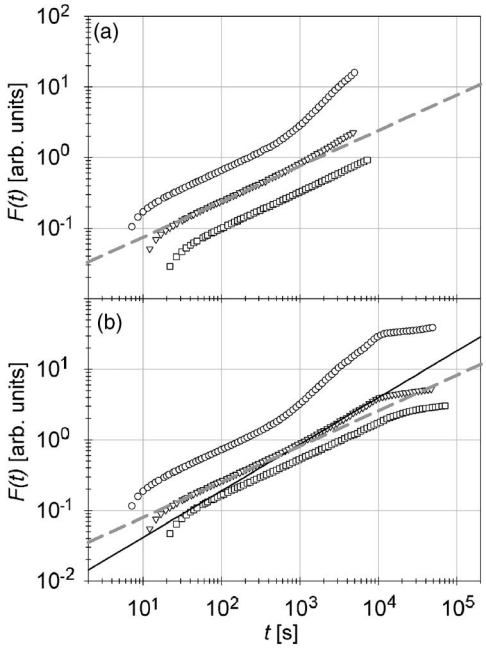

FIG. 5. DFA3 results for Al-9 at. % Zn at 0 °C. Double-logarithmic plot. Dashed gray lines indicate $\alpha=1/2$. (a) Typical fluctuation functions for three different scattering vectors: $Q/Q_{max}=1.04$ (○), $Q/Q_{max}=2.02$ (▽), and $Q/Q_{max}=3.07$ (□). (b): Typical fluctuation functions for time series consisting of concatenated time series from 10 consecutive pixels. That is, if p pixels are contained in a 20-pixel-wide annulus, $p/10$ (which is an integer) fluctuation functions of time series of length $N'=10N$ are calculated, each consisting of 10 concatenated time series of length N from consecutive pixels. The plotted $F(t)$ represents the average of the so-obtained $p/10$ fluctuation functions. Scattering vectors are the same as in (a). Note the improved statistics in the $\alpha>1/2$ range, which can be well fitted now. For the sake of clarity, only the fit for the middle curve is shown, full black line, yielding $\alpha\approx 0.66$.

The data evaluation was done for 20-pixel-wide annuli, each attributed to a certain Q value. For each pixel in such an annulus, DFA fluctuation functions were calculated and finally averaged. Figure 5(a) shows typical DFA3 fluctuation functions for the Al-9 at. % Zn data, taken at small, intermediate, and large scattering vectors.

On time scales up to almost half of the measurement time, $\alpha\approx 1/2$ is found due to uncorrelated noise in the data. Then, a crossover to $\alpha>1/2$ is observed. A further crossover to $\alpha\approx 1/2$ again is not seen.

In general, the DFA method shows a much larger initial regime with $\alpha\approx 1/2$ (corresponding to uncorrelated noise) than the FA method; see, e.g., the FA curves for Al-6 at. % Ag in Ref. [12], for comparison. The reason is that crossovers are shown more sharply by the DFA fluctuation functions that can also exhibit larger slopes in the double-logarithmic plot. Additionally, the following crossover to $\alpha>1/2$ is shifted to larger and larger time scales with each order of detrending [24]. As a consequence, a fit of the $\alpha>1/2$ region in Fig. 5(a) is statistically not reasonable. In order to find a remedy, one can analyze concatenated time series of consecutive pixels. That is, if p pixels are contained in a 20-pixel-wide annulus, one calculates $p/10$ (which is an integer) fluctuation functions of time series of length $N'=10N$, each consisting of 10 concatenated time series of length N from consecutive pixels. Finally, the so-obtained $p/10$ fluctuation functions are averaged. This procedure enlarges the $\alpha>1/2$ region and improves the statistics. In order to avoid jumps between the parts of the concatenated series, each part is multiplied by a constant number, so that its first value is identical with the last value of the previous one. Figure 5(b) shows the DFA3 results for time series consisting of 10 concatenated time series of consecutive pixels. The statistics of the $\alpha>1/2$ region appears to be well improved, making reasonable fitting possible; compare the full black line in Fig. 5(b).

When fitting our data, the upper limit for the fit range was given by the length of the time vector of a single pixel, i.e., 10% of the concatenated time series. The lower fit-range limit was determined by the crossover from uncorrelated ($\alpha=1/2$) to correlated behavior ($\alpha>1/2$) in the fluctuation function for the smallest Q/Q_{max} value and was kept constant for all further Q/Q_{max}.

If the parts of the concatenated time series were completely uncorrelated, the DFA would yield $\alpha=1/2$ for time scales larger than the measurement time. However, the fluctuation exponent obtained on very long time scales seems to be approximately zero. Most probably, this behavior comes from the spatial correlations between neighboring pixels. Since the speckle size was estimated to be slightly larger than one pixel, the time series of neighboring pixels are not completely independent. Rather, there is a periodicity in the concatenated series, the period time being the total recording time. Periodic series, however, exhibit $\alpha=0$ on scales larger than their period [42].

From Fig. 5(b), we may already infer that the dependence of the DFA3 fluctuation functions on the scattering vector Q/Q_{max} is qualitatively similar to the FA case, shown in Ref. [12]. For small scattering vectors ($Q/Q_{max}\approx 1$), the maximum α value is found and decreasing α values with increasing scattering vectors are obtained. Note, however, that in the DFA case, $\alpha>1$ can be detected.

Figure 6 shows the collected DFA3 results for the concatenated time series of Al-6 at. % Ag at 140 °C, full red circles, and Al-9 at. % Zn, full red triangles.

The dependence of α on Q/Q_{max} indicates high persistence on long length scales in real space, with the maximum at $Q/Q_{max}\approx 1$. Since our measurements were done under quasiequilibrium conditions, the mean precipitate interdistance stayed constant during the measurements. Thus the highest persistence is expected for $Q/Q_{max}\approx 1$. What is interesting is the fact that in the case of Al-6 at. % Ag at 140 °C, the α values are greater than 1, indicating an enhanced persistence [43] that causes nonstationary fluctuations that yield α values almost as high as for random-walk dynamics ($\alpha=1.5$). In the case of Al-9 at. % Zn at 0 °C, a qualitatively different coarsening dynamics is already indicated by the dramatically different fluctuation exponent for $Q/Q_{max}\approx 1$, where α does not exceed 1. This is a clear deviation from the pictures we obtained in our study of simulated data (see Sec. II), where only regimes with $\alpha=1/2$ (due to noise or fast dynamics) or $\alpha=3/2$ (due to a random walk of phases) were observed in addition to intermediate cross-

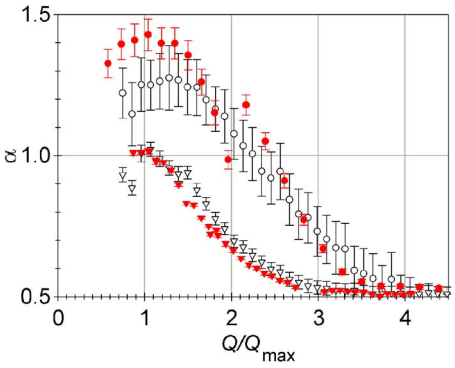

FIG. 6. (Color online) Fluctuation exponent α from DFA3 vs $Q/Q_{\max}$. Al-6 at. % Ag at 140 °C, full red circles. Al-9 at. % Zn at 0 °C, full red triangles. Fluctuation exponents from MC simulations [5]: Coarsening via LSW mechanism with scaled intensity plus background, open black circles. Coarsening via coagulation mechanism with scaled intensity plus background, open black triangles. The agreement between the LSW and the Al-6 at. % Ag data, and the coagulation and the Al-9 at. % Zn data is good, even quantitatively. Error bars indicate fit errors.

over regimes. Hence, our result of $\alpha=1$ for $Q\approx Q_{\max}$ seems to suggest that the dynamics of Al-9 at. % Zn on large length scales in real space might indeed not be characterized by random-walk processes, i.e., by diffusion. Instead, the value $\alpha\approx 1$ is characteristic of $1/f$ noise, which is ubiquitous in nature and often considered as a signature of self-organized criticality [44]. The difference between the $\alpha(Q/Q_{\max})$ curves is further pronounced for midrange $Q/Q_{\max}$, where the Al-6 at. % Ag curve lies considerably above the Al-9 at. % Zn curve. For large $Q/Q_{\max}$, both curves decay to $\alpha=1/2$, indicating only random uncorrelated fluctuations.

The open black symbols in Fig. 6 represent simulation results—open black circles for coarsening via the LSW mechanism and open black triangles for a predominant coagulation mechanism. In order to emulate the experimental conditions, the maximum simulation intensity was scaled to the maximum experimental intensities and, additionally, noise was introduced to account for the incoherent background [12]. Corresponding to the experimental data, this causes different signal-to-noise ratios in the simulated data. Note that the different signal-to-noise ratios may affect the fluctuation-function shape and thus the effectively determined α values, as was shown in Sec. II. Thus, different $\alpha(Q/Q_{\max})$ curves may be obtained from simulations with different signal-to-noise ratios, even if there is always the same coarsening mechanism employed. An extreme example for this behavior can be found in Ref. [45]. There, quite different $\alpha(Q/Q_{\max})$ curves are derived from simulated data as well as from experimental data for systems showing the same predominant coarsening mechanisms as in the present study, but having quite different signal-to-noise ratios. Since modest signal-to-noise ratios cause a broad initial $F(t)$ regime of $\alpha=1/2$, the determined α values were quite small in that case [45]. Also note that in Ref. [45], the FA technique was used for calculating fluctuation functions $F(t)$. Thus, the maximum α value detectable was 1, and possible crossovers in $F(t)$, from an initial uncorrelated regime($\alpha=1/2$) to a correlated regime ($\alpha>1/2$), appeared quite broad, in principle.

Coming back to Fig. 6, the rather large error bars from the fits of the simulation data are caused by the fact that simulated speckle patterns are available for only 100 time steps, since the quasiequilibrium condition had to be fulfilled also in the Monte Carlo simulations [5]. Since crossovers in the fluctuation functions are shifted to later time scales with higher detrending orders [24], the statistical significance of the parts of the DFA3 fluctuation functions that govern the true correlation behavior is limited for the simulation data.

Nevertheless, the agreement between the experimental and simulation curves is good, even quantitatively. Note that in contrast to the FA results presented in Ref. [12], the $\alpha(Q/Q_{\max})$ curves from DFA3 need not be scaled to each other in order to enable a better comparability. Further note that since crossovers appear sharper in fluctuation functions from DFA than from FA, fitting over crossovers in DFA3-fluctuation functions can be avoided, usually. Thus, it is not surprising that the $\alpha(Q/Q_{\max})$ curve for Al-9 at. % Zn exhibits greater α values than was found in Ref. [12]. In the case of Al-6 at. % Ag, the DFA3 evaluation yielded maximum α values greater than 1 that could not be detected with FA, in principle.

The results suggest that coarsening in Al-6 at. % Ag at 140 °C proceeds via the well-known LSW mechanism, whereas in Al-9 at. % Zn at 0 °C precipiate coagulation is predominant. A rough estimate where vacancies are preferably found in the two systems supports this conclusion. For this purpose, the melting temperatures T_m of the alloy constituents are considered [4]. If the melting point of the precipitating constituent is lower than that of the matrix, vacancies will rather be found in the precipitates than in the matrix, and vice versa. Having $T_m^{\mathrm{Al}}=933$ K, $T_m^{\mathrm{Ag}}=1234$ K, and $T_m^{\mathrm{Zn}}=693$ K gives a hint for a more prominent role of the coagulation mechanism in Al-9 at. % Zn than in Al-6 at. % Ag.

On the other hand, the picture for understanding the different shape of the $\alpha(Q/Q_{\max})$ curves for different coarsening mechanisms, which has already been derived from the FA results [12], still holds: At medium values of $Q/Q_{\max}$, structures in real space are probed on a length scale that compares to the average precipitate size. Precipitate movement, in the case of coarsening via coagulation, implies rather strong shape changes of single precipitates due to the rearrangement of atoms on precipitate surfaces, whereas in the LSW case the shape of single precipitates remains practically unchanged when single atoms evaporate from and condense on precipitate surfaces. Consequently, intensity fluctuations are less correlated for the coagulation mechanism, and smaller α values than for the LSW mechanism are obtained. At small scattering vectors, structures in real space are probed on even larger length scales. There, no details of precipitate shape—particularly no shape changes—are visible, which yields higher correlated signals. In the case of coarsening via the LSW mechanism, the structural rearrangement of the precipitates is characterized by diffusive motion (random-walk behavior) with very high persistence such that the fluctuations are nonstationary and α values greater than 1

are observed. In the case of coarsening via the coagulation mechanism, on the other hand, the diffusive motion seems to be replaced by $1/f$ fluctuations, which are exactly on the border line of stationarity and nonstationarity and are reminiscent of self-organized criticality [44]. At high $Q/Q_{\max}$, the dynamics is probed on very short length scales in real space, where smaller and smaller fluctuation exponents α indicate less and less correlated behavior for both the LSW and the coagulation mechanism dominating.

In conclusion, we presented in detail how detrended fluctuation analysis (DFA) can be used to analyze data of an x-ray photon correlation spectroscopy (XPCS) experiment. In this way, coarsening dynamics in phase-separating alloys at late stages of phase separation is studied. We not only confirm the qualitative findings for different coarsening mechanisms in Al-6 at. % Ag at 140 °C and Al-9 at. % Zn at 0 °C [12], but we actually find good quantitative agreement between experimental and simulation results. Thus, XPCS in combination with DFA represents a unique possibility for unambiguously identifying coarsening mechanisms in phase-separating alloys.

ACKNOWLEDGMENTS

We thank the staff of ID10A at the ESRF, Grenoble—in particular F. Zontone—for assistance during the measurements. This work was financially supported by the Austrian Federal Ministry for Education, Science and Culture (Project No. GZ 45.529/2-VI/B/7a/2002), the Austrian Science Fund (FWF) (Project No. P17775-N02), the EU Specific Targeted Research Project DYNASYNC (Project No. NMP4-CT-2003-001516), and the German Research Foundation (DFG) (SFB 418, Project No. B16). Data were evaluated using the Schrödinger II(I) cluster of the Vienna University Computer Center.

[1] J. L. Lifshitz and V. V. Slyozov, J. Phys. Chem. Solids **19**, 35 (1961).
[2] C. Wagner, Z. Elektrochem. **65**, 581 (1961).
[3] J.-M. Roussel and P. Bellon, Phys. Rev. B **73**, 085403 (2006).
[4] J.-M. Roussel and P. Bellon, Phys. Rev. B **63**, 184114 (2001).
[5] R. Weinkamer and P. Fratzl, Europhys. Lett. **61**, 261 (2003).
[6] K. Binder and D. Stauffer, Phys. Rev. Lett. **33**, 1006 (1974).
[7] N. Akaiwa and P. W. Voorhees, Phys. Rev. E **49**, 3860 (1994).
[8] K. Binder and D. W. Heermann, in *Scaling Phenomena in Disordered Systems*, edited by R. Pynn and A. Skjeltorp (Plenum Press, New York, 1985).
[9] R. Wagner, R. Kampmann, and P. W. Voorhees, in *Phase Transformation in Materials*, edited by G. Kostorz (Wiley-VCH Verlag, Weinheim, Germany, 2001).
[10] M. Sutton, S. G. J. Mochrie, T. Greytak, S. E. Nagler, L. E. Berman, G. A. Held, and G. B. Stephenson, Nature (London) **352**, 608 (1991).
[11] G. Grübel and F. Zontone, J. Alloys Compd. **362**, 3 (2004).
[12] Lorenz-M. Stadler, B. Sepiol, R. Weinkamer, M. Hartmann, P. Fratzl, J. W. Kantelhardt, F. Zontone, G. Grübel, and G. Vogl, Phys. Rev. B **68**, 180101(R) (2003).
[13] A. Fluerasu, M. Sutton, and E. M. Dufresne, Phys. Rev. Lett. **94**, 055501 (2005).
[14] K. Ludwig, F. Livet, F. Bley, J.-P. Simon, R. Caudron, D. LeBolloch, and A. Moussaid, Phys. Rev. B **72**, 144201 (2005).
[15] F. Livet, F. Bley, R. Caudron, E. Geissler, D. Abernathy, C. Detlefs, G. Grübel, and M. Sutton, Phys. Rev. E **63**, 036108 (2001).
[16] S. B. Dierker, R. Pindak, R. M. Fleming, I. K. Robinson, and L. Berman, Phys. Rev. Lett. **75**, 449 (1995).
[17] T. Thurn-Albrecht, W. Steffen, A. Patkowski, G. Meier, E. W. Fischer, G. Grübel, and D. L. Abernathy, Phys. Rev. Lett. **77**, 5437 (1996).
[18] T. Thurn-Albrecht, F. Zontone, G. Grübel, W. Steffen, P. Müller-Buschbaum, and A. Patkowski, Phys. Rev. E **68**, 031407 (2003).
[19] C.-K. Peng, S. V. Buldyrev, A. L. Goldberger, S. Havlin, F. Sciortino, M. Simons, and H. E. Stanley, Nature (London) **356**, 168 (1992).
[20] C.-K. Peng, S. V. Buldyrev, S. Havlin, M. Simons, H. E. Stanley, and A. L. Goldberger, Phys. Rev. E **49**, 1685 (1994).
[21] E. Koscielny-Bunde, A. Bunde, S. Havlin, H. E. Roman, Y. Goldreich, and H.-J. Schellnhuber, Phys. Rev. Lett. **81**, 729 (1998).
[22] A. Bunde, S. Havlin, J. W. Kantelhardt, T. Penzel, J.-H. Peter, and K. Voigt, Phys. Rev. Lett. **85**, 3736 (2000).
[23] Y. Liu, P. Cizeau, M. Meyer, C.-K. Peng, and H. E. Stanley, Physica A **245**, 437 (1997).
[24] J. W. Kantelhardt, E. Koscielny-Bunde, H. H. A. Rego, S. Havlin, and A. Bunde, Physica A **295**, 441 (2001).
[25] Lorenz-M. Stadler, B. Sepiol, J. W. Kantelhardt, I. Zizak, G. Grübel, and G. Vogl, Phys. Rev. B **69**, 224301 (2004).
[26] H. A. Makse, S. Havlin, M. Schwartz, and H. E. Stanley, Phys. Rev. E **53**, 5445 (1996).
[27] J. W. Goodman, *Statistical Optics* (John Wiley & Sons, Inc., New York, 1985).
[28] Z. Chen, P. C. Ivanov, K. Hu, and H. E. Stanley, Phys. Rev. E **65**, 041107 (2002).
[29] D. L. Abernathy, G. Grübel, S. Brauer, I. McNulty, G. B. Stephenson, S. G. J. Mochrie, A. R. Sandy, N. Mulders, and M. Sutton, J. Synchrotron Radiat. **5**, 37 (1998).
[30] O. K. C. Tsui, S. G. J. Mochrie, and L. E. Berman, J. Synchrotron Radiat. **5**, 30 (1998).
[31] F. Livet, F. Bley, A. Létoublon, J. P. Simon, and J. F. Bérar, J. Synchrotron Radiat. **5**, 1337 (1998).
[32] F. Langmayr, P. Fratzl, and G. Vogl, Acta Metall. Mater. **40**, 3381 (1992).
[33] G. Bischof, V. Grger, G. Krexner, and R. M. Nieminen, J. Phys.: Condens. Matter **8**, 7523 (1996).
[34] K. Osamura, H. Okuda, Y. Amemiya, and H. Hashizume, Metall. Trans. A **19A**, 1973 (1988).
[35] J. J. Hoyt and D. de Fontaine, Acta Metall. **37**, 1611 (1989).
[36] A. G. de Salva, J. P. Simon, F. Livet, and P. Guyot, Scr. Metall. **21**, 1061 (1987).

[37] T. T. Rautiainen and A. P. Sutton, Phys. Rev. B **59**, 13681 (1999).
[38] A. Malik, A. R. Sandy, L. B. Lurio, G. B. Stephenson, S. G. J. Mochrie, I. McNulty, and M. Sutton, Phys. Rev. Lett. **81**, 5832 (1998).
[39] A. Guinier and G. Fournet, *Small-Angle Scattering of X-rays* (Wiley, New York, 1955).
[40] H. Chen, S. Polat, and J. E. Epperson, in *Dynamics of Ordering Processes in Condensed Matter*, edited by S. Komura and H. Furukawa (Plenum Press, New York, 1988).
[41] D. Allen, S. Messoloras, R. J. Stewart, and G. Kostorz, J. Appl. Crystallogr. **11**, 578 (1978).
[42] K. Hu, P. C. Ivanov, Z. Chen, P. Carpena, and H. E. Stanley, Phys. Rev. E **64**, 011114 (2001).
[43] B. Pfau, L.-M. Stadler, B. Sepiol, R. Weinkamer, J. W. Kantelhardt, F. Zontone, and G. Vogl, Phys. Rev. B **73**, 180101(R) (2006).
[44] P. Bak, C. Tang, and K. Wiesenfeld, Phys. Rev. Lett. **59**, 381 (1987).
[45] Lorenz-M. Stadler, B. Sepiol, B. Pfau, G. Vogl, and F. Zontone, Nucl. Instrum. Methods Phys. Res. B **238**, 189 (2005).